

Phot1x Report

Marina Zajnulina, 30. November 2025

Abstract: Silicon photonics enables compact, low-loss, and CMOS-compatible integrated optical components, providing a powerful platform for the realization of interferometers, resonators, and wavelength-selective filters. In this work, I design, simulate, fabricate, and characterize three key passive photonic devices: Mach-Zehnder interferometers (MZIs), ring resonators, and Bragg gratings. These devices are implemented on a silicon-on-insulator (SOI) platform. Each device type is explored in multiple geometrical configurations, including different path imbalances for the MZIs, varying radii for the ring resonators, a dual-ring cascade for filter enhancement, and numerous grating periods and corrugation widths for the Bragg gratings. Using Lumerical INTERCONNECT and Mode for modelling and a NanoSOI multi-project wafer process for fabrication (Applied Nanotools Inc.), the study examines how structural parameters influence the free spectral range, group index, and filtering behaviour. The fabricated devices are subsequently characterized using a tunable-laser measurement setup to compare experimental performance with theoretical predictions and simulation results, providing a complete design-to-measurement validation of SOI photonic components.

1 Introduction

This study aims to design, fabricate, and evaluate the performance of three different photonic devices, Mach-Zehnder Interferometers (MZIs), passive ring resonators, and Bragg gratings, in three different configurations, each using silicon-on-insulator (SOI) technology. Thus, the MZIs have different path lengths, the ring resonators different radii, and the Bragg gratings different grating periods or corrugation widths. Additionally, one device contains a series of two ring resonators to see how such a configuration influences the transmission behaviour and whether it can be used as a filter. The layout of the chip containing all devices and submitted for fabrication is shown in Fig. 1.1.

The considered MZI path length difference is $\Delta l_1 = 10.2 \mu\text{m}$, $\Delta l_2 = 25.316 \mu\text{m}$, and $\Delta l_3 = 62.577 \mu\text{m}$.

The radii of the ring resonators are $R_1 = 5 \mu\text{m}$, $R_2 = 7 \mu\text{m}$, and $R_3 = 11 \mu\text{m}$. The configuration of two ring resonators in series has the radii $R_{4/1} = 11 \mu\text{m}$ and $R_{4/2} = 7 \mu\text{m}$. The gaps between the bus waveguide and the ring resonator are $0.11 \mu\text{m}$ for all configurations.

All Bragg gratings have the same number of periods, namely 300. The first grating has a grating period of $GP_1 = 0.317 \mu\text{m}$ and corrugation width

of $CW_1 = 0.05 \mu m$, the second one $GP_2 = 0.315 \mu m$ and $CW_2 = 0.05 \mu m$, and the third one $GP_3 = 0.317 \mu m$ and $CW_3 = 0.1 \mu m$.

All devices utilize standard waveguides with a width of $0.5 \mu m$ and a height of $0.22 \mu m$. The devices are designed to operate in the TE mode at a central wavelength of $1550 nm$.

2 Theory

Assuming 50/50 couplers, the transfer function for an unbalanced MZI with identical waveguides, i.e., waveguides with equal propagation constant β , is

$$I_o = \frac{I_i}{2}[1 + \cos(\beta\Delta l)] \quad (1)$$

with I_o and I_i being the output and input intensity, respectively, and Δl the path length difference in the arms of the interferometer. The corresponding free spectral range (FSR) reads as:

$$FSR = \frac{\lambda^2}{n_g \Delta l} \quad (2)$$

with a wavelength-dependent group index

$$n_g(\lambda) = n_{eff} - \lambda \frac{dn_{eff}}{d\lambda}, \quad (3)$$

where n_{eff} is the effective index of the material.

For a passive ring resonator with a radius R , the free spectral range reads as:

$$FSR = \frac{\lambda^2}{n_g 2\pi R}. \quad (4)$$

For Bragg gratings, deriving and understanding the transmission formula that includes the grating period and corrugation width as parameters requires exhaustive theoretical considerations beyond the scope of this study. Therefore, the dependence of the grating performance on these parameters will be considered phenomenologically in Sec. 3.

3 Modelling and Simulation

The simulations to calculate the transmission behaviour of the devices depicted in Fig. 1.1 are performed using commercial software Lumerical INTERCONNECT.

3.1 The Free Spectral Range of Mach-Zehnder Interferometers

The free spectral range is determined as the difference between two neighbouring minima in the gain spectrum of the considered device. The temperature is set to $T = 300 K$.

Using simulations and reading out values around the central wavelength of $1550 nm$, the following FSR values were achieved for MZIs with various path lengths $\Delta l_i, i = 1, 2, 3$:

$$FSR_1(\Delta l_1 = 10.2 \mu m) = 62.13 nm \quad (5)$$

$$FSR_2(\Delta l_2 = 25.316 \mu m) = 23.45 nm \quad (6)$$

$$FSR_3(\Delta l_3 = 62.577 \mu m) = 9.22 nm \quad (7)$$

which is in line with Eq. 1, meaning that an increasing path length difference results in a decreasing free spectral range. An example of the gain spectrum for $\Delta l_3 = 62.577 \mu m$ is given in Fig. 3.1.

3.2 The Free Spectral Range of Ring Resonators

To simulate the transmission spectrum of the ring resonators, I chose the option "Find the nearest S parameters". The

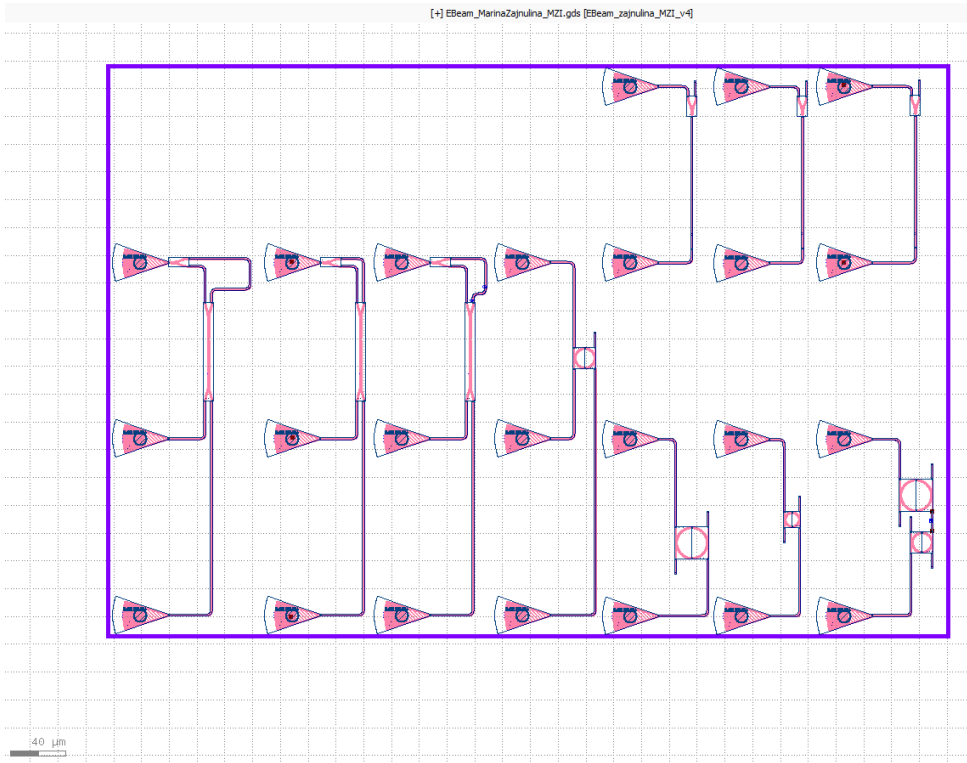


Figure 1.1 Chip layout submitted for fabrication.

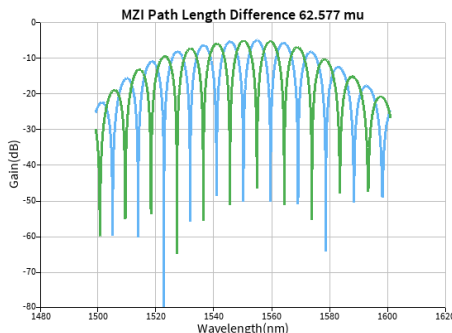


Figure 3.1 Example of a simulated gain spectrum at output arms of an unbalanced Mach-Zehnder Interferometer with 50/50 input and output couplers and path length difference of $\Delta l_3 = 62.577 \mu m$. The temperature of simulations is set to $T = 300 K$, i.e. $T = 26.85^\circ C$.

following values were achieved:

$$\begin{aligned} FSR_1(R_1 = 5 \mu m) &= 18.84 nm \\ FSR_2(R_2 = 7 \mu m) &= 18.79 nm \\ FSR_3(R_3 = 11 \mu m) &= 9.28 nm. \end{aligned}$$

As we see, the values of R_1 and R_2 are too close to each other to significantly influence the resonant condition and, thus, the free spectral range. Therefore, the corresponding FSR-values are almost identical. However, the distortion of the spectrum for R_2 as compared with the spectrum for R_1 shows that the ring resonator radius of $R_2 = 7 \mu m$ is close to leaving the resonant condition (Fig. 3.2). A comparison of FSR_1 and FSR_3 shows that these values are in line with Eq. 4,

meaning that a greater ring resonator radius results in a smaller free spectral range.

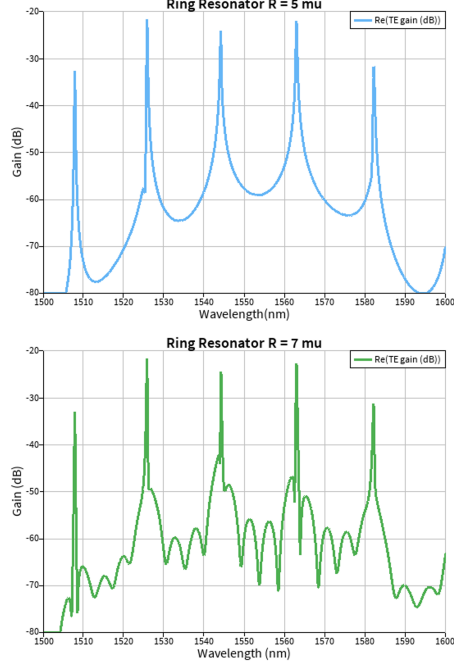


Figure 3.2 Gain spectrum of passive ring resonators with radii $R_1 = 5 \mu m$ and $R_2 = 7 \mu m$.

3.3 The Free Spectral Range of Ring Resonators in Series

Connecting two ring resonators with radii $R_{4/1} = 11 \mu m$ and $R_{4/2} = 7 \mu m$ in series yields a gain spectrum similar to a double comb, with a greater free spectral range of $18.35 \mu m$ and a smaller free spectral range between two neighbouring comb teeth of $1.82 \mu m$ (Fig. 3.3).

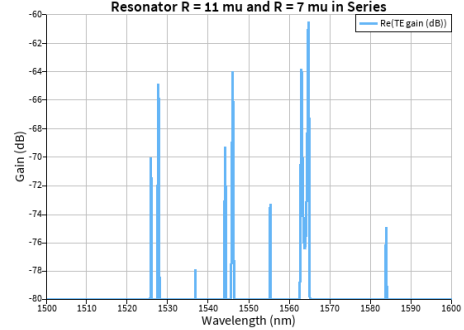


Figure 3.3 Gain spectrum of passive ring resonators with radii $R_{4/1} = 11 \mu m$ and $R_{4/2} = 7 \mu m$ connected in series.

3.4 Detailed Free Spectral Range and Group Index Simulations of a MZI Device

Here, I present the FSR and group index profiles of an MZI with a path length difference of $\Delta l_3 = 62.577 \mu m$. The simulations are performed using Lumerical INTERCONNECT accessed through the KLayout file (cf. Fig. 1.1, left corner, Fig. 3.1). The temperature was set to $T = 300 K$. The plots were done using MS Excel. The group index was calculated using Eq. 3.

According to Fig. 3.4, the free spectral range is $FSR_3 = 9.22 nm$ and the group index $GP_3 = 4.17$ at wavelength of $\lambda = 1550.32 nm$, which is in line with the FSR achieved by reading out the minimal values of the gain spectrum (Eq. 7).

3.5 Bragg Grating Transmission Profile Depending On Grating Period

The numerical studies of the transmission profile of Bragg gratings are performed using a temperature value of $T = 300 K$.

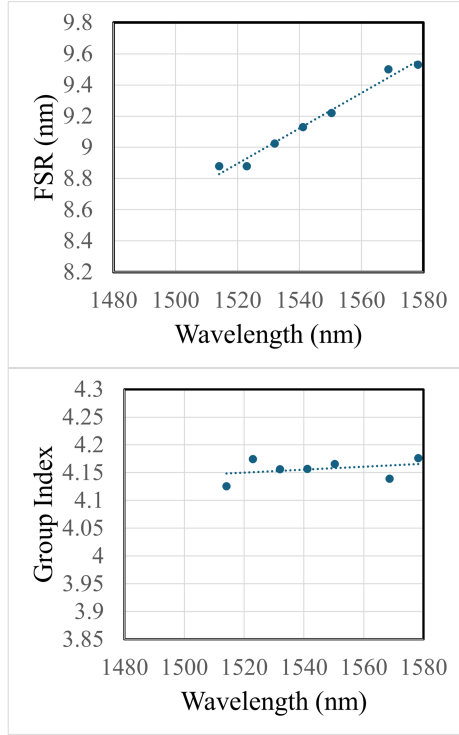


Figure 3.4 Simulated free spectral range and group index of an unbalanced Mach-Zehnder Interferometer with 50/50 input and output couplers and path length difference of $\Delta l_3 = 62.577 \mu m$. The temperature of simulations is set to $T = 300 K$, i.e. $T = 26.85^{\circ}C$.

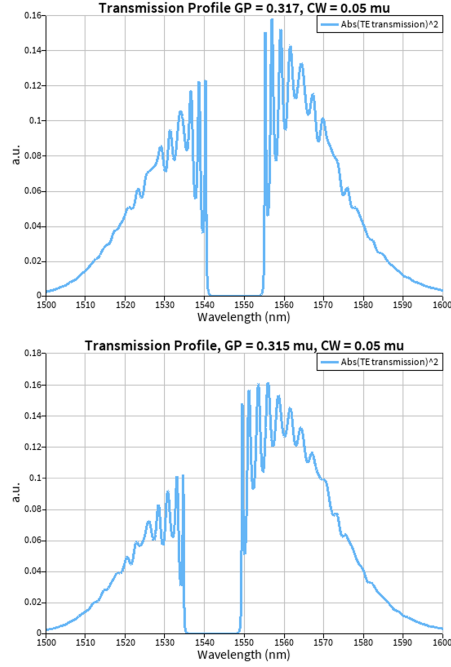


Figure 3.5 Transmission profiles of two Bragg gratings with grating periods of $GP_1 = 0.317 \mu m$ and $GP_2 = 0.315 \mu m$ and the same value of the corrugation width.

telecom wavelength of $1550 nm$, the grating period of $GP_1 = 0.317 \mu m$ should be chosen (Fig. 3.5).

Fig. 3.5 shows the transmission profiles of two Bragg gratings with grating periods of $GP_1 = 0.317 \mu m$ and $GP_2 = 0.315 \mu m$. Both gratings have the same corrugation width of $CW_1 = CW_2 = 0.05 \mu m$. A comparison of the transmission profiles shows that the grating period significantly affects the notch spectral position. Thus, increasing the grating period shifts the notch towards the longer IR wavelengths, which can be exploited when designing filters. For applications that seek to filter out the

3.6 Bragg Grating Transmission Profile Depending On Corrugation Width

Fig. 3.6 shows how the corrugation width impacts the notch depth. Thus, a larger corrugation width yields a deeper notch with sharper slopes, which can be exploited to cover a broader wavelength range and filter out.

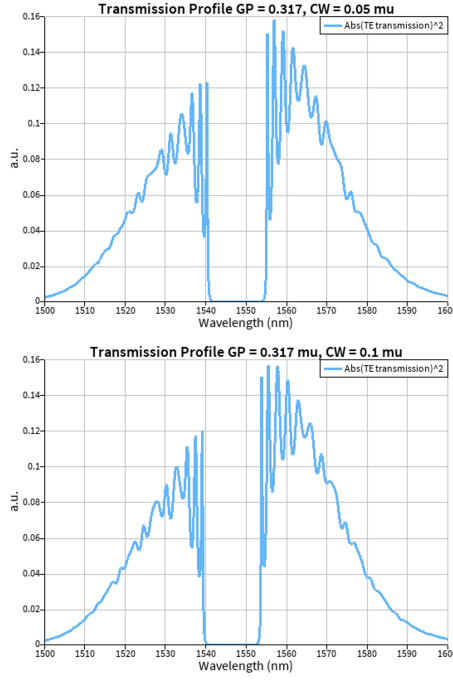


Figure 3.6 Transmission profiles of two Bragg gratings with the same grating period of $GP_1 = GP_3 = 0.317 \mu m$, but different values of the corrugation width, $CW_1 = 0.05 \mu m$ and $CW_3 = 0.1 \mu m$.

3.7 Corner Analysis of a Mach-Zehnder Interferometer

To account for manufacturing variability, I performed a corner analysis assuming a variability of waveguide dimensions of $\pm 5\%$, which results in a waveguide width range of $475 - 525 nm$ and a height range of $209 - 231 nm$. The simulations were performed using Lumerical INTERCONNECT and Lumerical MODE at a device temperature of $T = 300 K$. The device that was used is a MZI with $\Delta l_3 = 62.577 \mu m$ (cf. Fig. 1.1, left corner, Fig. 3.1). The group index was calculated using Eq. 3.

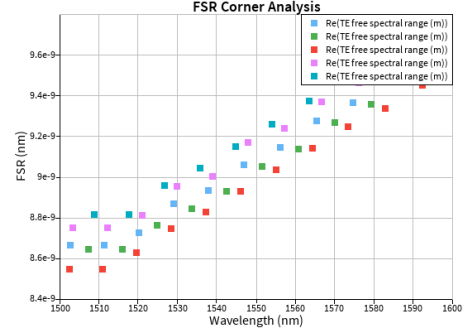


Figure 3.7 Simulated variation of the free spectral range due to the variability of the waveguide dimensions of $\pm 5\%$ for an MZI with a path length difference of $\Delta l_3 = 62.577 \mu m$ at a temperature of $T = 300 K$.

According to Fig. 3.7, the group index range achieved by corner analysis is $4.17 - 4.28$ at wavelength of $1550 nm$.

4 Fabrication: Applied Nanotools, Inc. NanoSOI Process

The photonic devices were fabricated using the NanoSOI MPW fabrication process by Applied Nanotools Inc. (<http://www.appliednt.com/nanosoi>; Edmonton, Canada) which is based on direct-write 100 keV electron beam lithography technology. Silicon-on-insulator wafers of 200 mm diameter, 220 nm device thickness and 2 μm buffer oxide thickness are used as the base material for the fabrication. The wafer was pre-diced into square substrates with dimensions of 25x25 mm, and lines were scribed into the substrate backsides to facilitate easy separation into smaller chips once fabrication was complete. After an initial wafer clean using piranha solution (3:1 H₂SO₄:H₂O₂) for 15 minutes and water/IPA rinse, hydrogen silsesquioxane (HSQ) resist was spin-coated onto

the substrate and heated to evaporate the solvent. The photonic devices were patterned using a Raith EBPG 5000+ electron beam instrument using a raster step size of 5 nm. The exposure dosage of the design was corrected for proximity effects that result from the backscatter of electrons from exposure of nearby features. Shape writing order was optimized for efficient patterning and minimal beam drift. After the e-beam exposure and subsequent development with a tetramethylammonium sulfate (TMAH) solution, the devices were inspected optically for residues and/or defects. The chips were then mounted on a 4" handle wafer and underwent an anisotropic ICP-RIE etch process using chlorine after qualification of the etch rate. The resist was removed from the surface of the devices using a 10:1 buffer oxide wet etch, and the devices were inspected using a scanning electron microscope (SEM) to verify patterning and etch quality. A 2.2 μm oxide cladding was deposited using a plasma-enhanced chemical vapour deposition (PECVD) process based on tetraethyl orthosilicate (TEOS) at 300°C. Reflectometry measurements were performed throughout the process to verify the device layer, buffer oxide and cladding thicknesses before delivery.

5 Experimental Data

To characterize the devices, a custom-built automated test setup with automated control software written in Python was used (<http://siepic.ubc.ca/probestation>). An Agilent 81600B tunable laser was used as the input source and Agilent 81635A optical power sensors as the output detectors. The wavelength was swept from 1500 to 1600 nm in 10

pm steps. A polarization maintaining (PM) fibre was used to maintain the polarization state of the light, to couple the TE polarization into the grating couplers A 90° rotation was used to inject light into the TM grating couplers [4]. A polarization maintaining fibre array was used to couple light in/out of the chip [www.plcconnections.com].

5.1 Missing MATLAB Optimization Tool

To evaluate the measurements in accordance with the task, I missed an Optimization MATLAB Toolbox (Fig. 5.1). I circumvented this problem by using Origin (OriginLab) for plotting the measurement data and reading out the free spectral range manually.

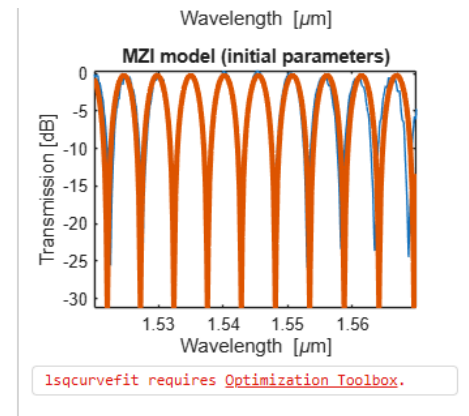


Figure 5.1 MATLAB error message about missing Optimization Toolbox.

5.2 Baseline Correction

Due to the limited bandwidth of the grating couplers, device transmission profiles (gain spectrum) might need a baseline correction. Fig. 5.2 is an example of a

baseline-corrected gain spectrum of an MZI with a path length difference of $\Delta l_3 = 62.577 \mu m$.

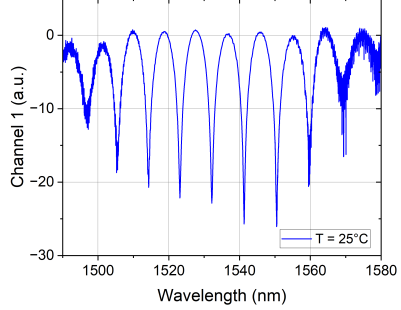


Figure 5.2 Measured baseline-corrected gain spectrum at one of the output arms (Channel 1) of an unbalanced Mach-Zehnder Interferometer with 50/50 input and output couplers and a path length difference of $\Delta l_3 = 62.577 \mu m$.

As the limitation in the bandwidth does not hinder reading out the free spectral range manually, I will omit this procedure in the next steps.

5.3 Temperature-Dependence of the Transmission Profiles: An MZI

In this subsection, I study the measured temperature dependence of the transmission profiles of an MZI. The device temperatures are $T = 25^\circ C, 30^\circ C, 35^\circ C$.

Fig. 5.3 shows the measured gain spectrum of the MZI with the path length difference of $\Delta l_3 = 62.577 \mu m$ (Fig. 3.1). As one can see, the shift of the peaks towards the infrared is nonlinear with temperature. Thus, an increase of the temperature from $T = 25^\circ C$ to $T = 30^\circ C$ results in a shift of only $0.35 nm$, whereas a step from $T = 30^\circ C$ to $T = 35^\circ C$ yields an increase of $1.8 nm$. At this MZI output

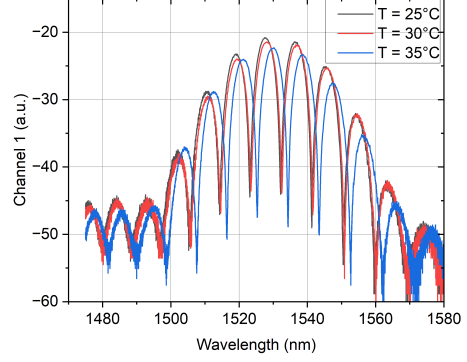


Figure 5.3 Measured gain spectrum at one of the output arms (Channel 1) of an unbalanced Mach-Zehnder Interferometer with 50/50 input and output couplers and a path length difference of $\Delta l_3 = 62.577 \mu m$ for three different temperatures.

arm, the gain spectrum has a minimum for $T = 25 - 30^\circ C$ at $\lambda = 1550 nm$, which indicates that another output arm should be used for an optimized transmission of this device.

5.4 Temperature-Dependence of the Transmission Profiles: A Bragg Grating

In this subsection, I study the measured temperature dependence of the transmission profiles of a Bragg grating. The device temperatures are $T = 25^\circ C, 30^\circ C, 35^\circ C$. Fig. 5.4 shows the measured transmission profile of a Bragg grating with grating period of $GP_1 = 0.317 \mu m$ and corrugation width of $CW_1 = 0.05 \mu m$. As one can see, there is no noticeable difference in the transmission profile at $T = 25^\circ C, 30^\circ C, 35^\circ C$. However, the center of the notch lies at ≈ 1542 which rather coincides with grating period of $GP_2 = 0.315 \mu m$ for the same corrugation width (Fig. 3.5). A possibly reduced grating period might be

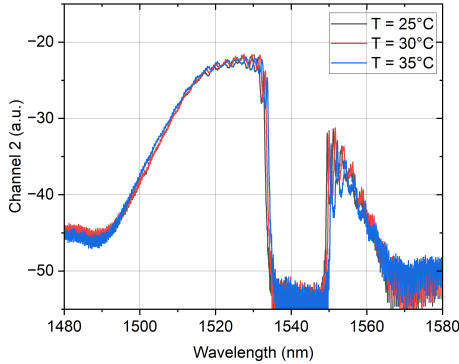


Figure 5.4 Measured transmission profile of a Bragg grating with a grating period of $GP_1 = 0.317 \mu\text{m}$ and a corrugation width of $CW_1 = 0.05 \mu\text{m}$ for three different temperatures $T = 25^\circ\text{C}, 30^\circ\text{C}, 35^\circ\text{C}$.

due to the increased dimensions of the waveguide (cf. Sec . 6).

6 Analysis

Fig. 6.1 shows the measured free spectral range and group index (cf. Eq. 3) of an MZI with a path length difference of $\Delta l_3 = 62.577 \mu\text{m}$ at device temperature of $T = 25^\circ\text{C}$ ($T = 298.15 \text{ K}$).

According to Fig. 6.1, the measured free spectral range is $FSR_3 = 9.33 \text{ nm}$ and the group index $GP_3 = 4.12$ at wavelength of $\lambda = 1550.472 \text{ nm}$ being beyond the range achieved by corner analysis (Sec. 3.7). There are three possible reasons for it. They have an additive action.

- The temperature of the simulations and the measurements is slightly different, which might have resulted in a slight difference between the effective and group refractive index, leading to an increased FSR value of the measured device.
- The closest corner-analysis value is for the waveguide width of 525 nm and a

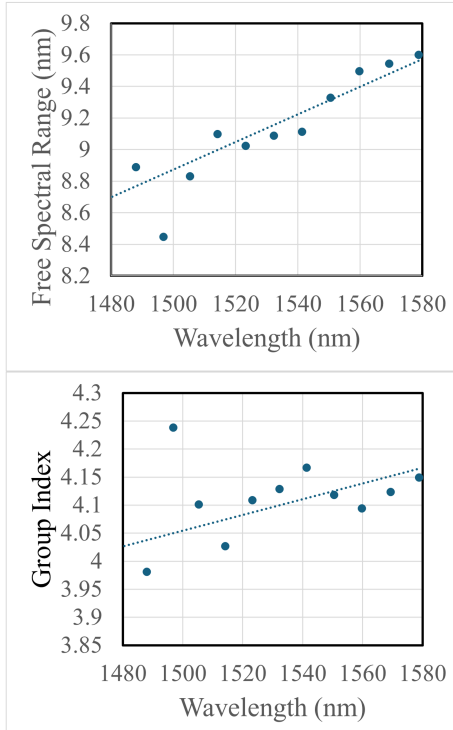


Figure 6.1 Measured free spectral range and group index of an unbalanced Mach-Zehnder Interferometer with 50/50 input and output couplers and path length difference of $\Delta l_3 = 62.577 \mu\text{m}$. The temperature is $T = 25^\circ\text{C}$.

height of 209 nm, indicating that the fabricated device is broader and has a smaller height than the ideal one with a waveguide width of 500 nm and a height of 220 nm.

- The final reason why the experimental results lie beyond the initial corner analysis lies in the fact that I, not having the MATLAB Optimization Toolbox, read out the FSR by hand, which might have introduced a considerable read-out error.

Taking into account all three possible reasons, an outlier of only 1.12 % (corresponding to the group index of 4.12) with

respect to the minimal corner-analysis value (4.17) is an acceptable result. As the minimal value of the group index (4.17) was achieved for a waveguide width of 525 nm and a height of 209 nm , I conclude that the measured device was also broader than 500nm , whereas its height was less than 220 nm .

7 Conclusion

This study presented the complete design, simulation, fabrication, and experimental characterization of several passive silicon photonic devices, including Mach-Zehnder interferometers, ring resonators, and Bragg gratings implemented on an SOI platform. The measured transmission spectra and free spectral ranges showed good agreement with theoretical predictions and simulation results, with discrepancies largely attributable to fabrication tolerances and manual FSR extraction. The corner analysis confirmed that slight variations in waveguide width and height can account for the observed shifts in group index. Bragg grating measurements further validated the expected dependence of notch position and depth on grating period and corrugation width.

8 Acknowledgements

I acknowledge the edX UBCx Phot1x Silicon Photonics Design, Fabrication and Data Analysis course, which is supported by the Natural Sciences and Engineering Research Council of Canada (NSERC) Silicon Electronic-Photonic Integrated Circuits (SiEPIC) Program. The devices were fabricated by Richard Bojko at the University of Washington Washington Nanofabrication Facility, part of the National Science Foundation's National Nanotechnology Infrastructure Network (NNIN), and Cameron

Horvath at Applied Nanotools, Inc. Enxiao Luan performed the measurements at The University of British Columbia. We acknowledge Lumerical Solutions, Inc., Mathworks, Mentor Graphics, Python, and KLayout for the design software.

References

1. Chrostowski L, Hochberg M (2015) Silicon Photonics Design. Cambridge University Press (CUP)
2. Bojko RJ, Li J, He L, et al. (2011) Electron beam lithography writing strategies for low loss high confinement silicon optical waveguides. Journal of Vacuum Science & Technology B: Microelectronics and Nanometer Structures 29:06F309. <https://doi.org/10.1116/1.3653266>
3. Chrostowski L, Hochberg M Testing and packaging. In: Silicon Photonics Design. Cambridge University Press (CUP), pp 381–405
4. Wang Y, Wang X, Flueckiger J, et al. (2014) Focusing sub-wavelength grating couplers with low back reflections for rapid prototyping of silicon photonic circuits. Opt Express 22:20652. <https://doi.org/10.1364/oe.22.020652>
5. Osgood R Jr, Meng X (2021) Principles of Photonic Integrated Circuits: Materials, Device Physics, Guided Wave Design. Springer
6. Wang Y, Wang X, Flueckiger J, et al. (2014) Focusing sub-wavelength grating couplers with low back reflections for rapid prototyping of silicon photonic circuits. Opt Express 22:20652. <https://doi.org/10.1364/oe.22.020652>
7. Ouyang B, Li Y, Kruidhof M, et al. (2019) On-chip silicon Mach-Zehnder interferometer sensor for ultrasound detection. Opt. Lett. 44, 1928–1931. <https://doi.org/10.1364/OL.44.001928>